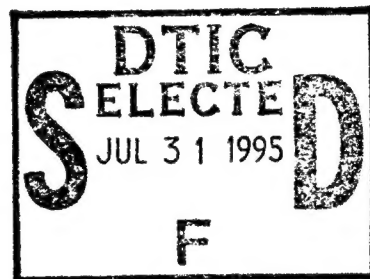


RL-TR-94-239
In-House Report
December 1994



ADAPTIVE OPTICAL RADIAL BASIS FUNCTION NEURAL NETWORK CLASSIFIER

Wesley E. Foor



APPROVED FOR PUBLIC RELEASE; DISTRIBUTION UNLIMITED.

DTIC QUALITY INSPECTED 5

Rome Laboratory
Air Force Materiel Command
Griffiss Air Force Base, New York

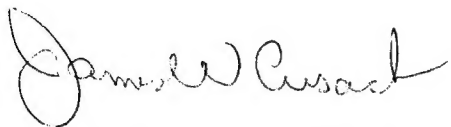
19950728 032

16K

This report has been reviewed by the Rome Laboratory Public Affairs Office (PA) and is releasable to the National Technical Information Service (NTIS). At NTIS it will be releasable to the general public, including foreign nations.

RL-TR-94-239 has been reviewed and is approved for publication.

APPROVED:



JAMES W. CUSACK, Chief
Photonics & Optics Division
Surveillance & Photonics Directorate

FOR THE COMMANDER:



DONALD W. HANSON
Director of Surveillance & Photonics

If your address has changed or if you wish to be removed from the Rome Laboratory mailing list, or if the addressee is no longer employed by your organization, please notify RL (OCPA) Griffiss AFB NY 13441. This will assist us in maintaining a current mailing list.

Do not return copies of this report unless contractual obligations or notices on a specific document require that it be returned.

REPORT DOCUMENTATION PAGE

Form Approved
OMB No. 0704-0188

Public reporting burden for this collection of information is estimated to average 1 hour per response, including the time for reviewing instructions, searching existing data sources, gathering and maintaining the data needed, and completing and reviewing the collection of information. Send comments regarding this burden estimate or any other aspect of this collection of information, including suggestions for reducing this burden, to Washington Headquarters Services, Directorate for Information Operations and Reports, 1215 Jefferson Davis Highway, Suite 1204, Arlington, VA 22202-4302, and to the Office of Management and Budget, Paperwork Reduction Project (0704-0188), Washington, DC 20503.

1. AGENCY USE ONLY (Leave Blank)		2. REPORT DATE December 1994	3. REPORT TYPE AND DATES COVERED In-House Oct 93 - Dec 94
4. TITLE AND SUBTITLE ADAPTIVE OPTICAL RADIAL BASIS FUNCTION NEURAL NETWORK CLASSIFIER		5. FUNDING NUMBERS PE - 62702F PR - 4600 TA - P1 WU - 13	
6. AUTHOR(S) Wesley E. Foor			
7. PERFORMING ORGANIZATION NAME(S) AND ADDRESS(ES) Rome Laboratory (OCPA) 25 Electronic Pky Griffiss AFB NY 13441-4515		8. PERFORMING ORGANIZATION REPORT NUMBER RL-TR-94-239	
9. SPONSORING/MONITORING AGENCY NAME(S) AND ADDRESS(ES) Rome Laboratory (OCPA) 25 Electronic Pky Griffiss AFB NY 13441-4515		10. SPONSORING/MONITORING AGENCY REPORT NUMBER N/A	
11. SUPPLEMENTARY NOTES Rome Laboratory Project Engineer: Wesley E. Foor/OCPA/(315) 330-2944			
12a. DISTRIBUTION/AVAILABILITY STATEMENT Approved for public release; distribution unlimited.		12b. DISTRIBUTION CODE	
13. ABSTRACT (Maximum 200 words) An adaptive optical radial basis function neural network classifier is experimentally demonstrated. We describe a spatially multiplexed system incorporating on-line adaptation of weights and basis function widths to provide robustness to optical system imperfections and system noise. The optical system computes the Euclidean distances between a 100-dimensional input vector and 198 stored reference patterns in parallel using dual vector-matrix multipliers and a contrast-reversing spatial light modulator. Software is used to emulate an analog electronic chip that performs the on-line learning of the weights and basis function widths. An experimental recognition rate of 92.7% correct out of 300 testing samples is achieved with the adaptive training versus 31.0% correct for non-adaptive training. We compare the experimental results with a detailed computer model of the system in order to analyze the influence of various noise sources on the system performance.			
14. SUBJECT TERMS Optical neural networks, radial basis functions, pattern recognition		15. NUMBER OF PAGES 48	16. PRICE CODE
17. SECURITY CLASSIFICATION OF REPORT UNCLASSIFIED	18. SECURITY CLASSIFICATION OF THIS PAGE UNCLASSIFIED	19. SECURITY CLASSIFICATION OF ABSTRACT UNCLASSIFIED	20. LIMITATION OF ABSTRACT UL

Contents

1	INTRODUCTION	1
2	RBF NEURAL NETWORKS FOR HANDWRITTEN DIGIT RECOGNITION	2
2.1	RBF Neural Networks	2
2.2	Handwritten Digit Recognition	5
3	OPTICAL RBF NEURAL NETWORK	8
3.1	Parallel Optical Distance Computation	8
3.2	Parallel Basis Function Evaluation	11
4	NOISE CHARACTERIZATION AND COMPUTER MODELING	14
4.1	Optical System Noise Characteristics	14
4.1.1	Illumination Characteristics	14
4.1.2	SLM Characteristics	15
4.1.3	LCLV Characteristics	15
4.1.4	System Noise Characteristics	17
4.1.5	Other Optical System Characteristics	17
4.2	Optical System Software Model	18
5	ADAPTIVE OPTICAL RBF NEURAL NETWORK	21
5.1	Adaptive Postprocessor	21
5.2	Influences of Noise on System Performance	21

5.3 Adaptive Optical RBF Neural Network Results 23

6 CONCLUSIONS AND FUTURE WORK 28

REFERENCES 30

Accesion For	
NTIS	CRA&I
DTIC	TAB
Unannounced	
Justification	
By _____	
Distribution / _____	
Availability Codes	
Dist	Avail and / or Special
A-1	

List of Figures

2.1	Schematic diagram of RBF neural network for digit recognition.	3
2.2	Illustration indicating the operation of the class-based clustering technique used to reduce the number of RBF center locations.	4
2.3	Samples of unprocessed 40x40 pixel digits.	6
2.4	Samples of centered and scaled 10x10 pixel digits.	6
2.5	Training history of software RBF neural network error.	7
3.1	Dual-rail vector-matrix multiplier used as a parallel optical distance computer. . . .	9
3.2	Picture of optical RBF classifier system.	10
3.3	Example of a centers mask (not to scale).	10
3.4	Euclidean distance vs. template number for a single input image (handwritten 0). a) Actual distance and b) optically computed distance.	11
3.5	Euclidean distance vs. template number for a single input image (handwritten 4). a) Actual distance and b) optically computed distance.	11
3.6	Non-adaptive RBF postprocessing chip for a single output network.	13
4.1	Measured and modeled LCLV transfer functions.	16
4.2	Measured intensity fluctuations over time measured on a $50 \mu m^2$ area of the LCLV. .	17
4.3	Image of the readout side of the LCLV depicting nonuniformities (slightly out of focus). .	19
5.1	Adaptive RBF postprocessing chip module.	22
5.2	Predicted recognition rate versus imaging axis beam profile. a) Otherwise ideal system. b) Incorporating all error sources.	24

5.3	Predicted recognition rate versus collimating axis beam profile. a) Otherwise ideal system. b) Incorporating all error sources.	24
5.4	Predicted recognition rate versus LCLV readbeam profile. a) Otherwise ideal system. b) Incorporating all error sources.	24
5.5	Predicted recognition rate versus finite SLM contrast. a) Otherwise ideal system. b) Incorporating all error sources.	25
5.6	Predicted recognition rate versus leg intensity ratio. a) Otherwise ideal system. b) Incorporating all error sources.	25

List of Tables

2.1	Results of clustering algorithm.	4
3.1	Performance comparison between optical RBF classifier and software RBF classifier.	12
4.1	Measured error values from optical system.	18
4.2	Performance comparison between optical RBF classifier and modeled optical RBF classifier.	20
5.1	Performance comparison between adaptive optical RBF classifier and the modeled adaptive optical RBF classifier.	26
5.2	Confusion matrix for adaptive optical RBF network.	27

1

INTRODUCTION

Adaptive neural networks are considered to be promising architectures for real-time pattern recognition. Due to the large network sizes required for real-world problems involving imagery, these adaptive networks will be most useful for solving real-time problems if they are implemented in parallel hardware. The parallel processing capabilities of opto-electronic systems together with the relatively simple computational requirements of artificial neural networks make optics a natural candidate for hardware implementations of neural computing systems. Optical computing systems however, typically suffer from optical device imperfections and system noise that can degrade performance. By employing adaptive on-line training techniques these noise sources can be incorporated into an error-driven learning process to provide improved system performance. Neural networks therefore offer an opportunity to realize parallel optical computing systems that tolerate noise. In this paper we describe an adaptive neural architecture capable of exploiting parallel optical hardware for multi-dimensional signal classification.

The radial basis function (RBF) neural network has been successfully used in many multi-dimensional classification applications including 3D object recognition [1, 2], radar signal classification [3], face recognition [4, 5], fingerprint recognition [6], speech recognition [7], and handwritten character recognition [8, 9]. Other applications of RBF neural networks include nonlinear function approximation [10, 11, 1], kernel regression [12], equalization of time-dispersive communication channels, and nonlinear modeling and prediction for echo cancellation in the presence of nonlinear distortion [13]. Previous experiments have shown that RBF networks have similar classification performance to backpropagation neural networks while typically incurring shorter training times [8]. Both all-electronic [14] and opto-electronic [15] parallel hardware implementations of RBF networks have been reported.

In this paper we experimentally demonstrate an adaptive optical RBF classifier that facilitates on-line learning to offer robustness to noise and optical system imperfections. The system performance is evaluated in the application of handwritten digit classification. The issues of system imperfections, device characterization, and system noise are discussed. The experimental results from our optical system are compared with data from a computer model of the system in order to identify critical noise sources and to indicate possible areas for system performance improvements. We then present conclusions and discuss future directions of this work.

RBF NEURAL NETWORKS FOR HANDWRITTEN DIGIT RECOGNITION

2.1 RBF Neural Networks

A single-output multi-layer neural network can be regarded as a continuous input-output mapping, $\mathbb{R}^N \rightarrow \mathbb{R}$. The network should behave well in the presence of noise and correctly generalize when a previously unseen input pattern is presented. To obtain these characteristics we may impose smoothing constraints on the input-output mapping as derived from regularization techniques and approximation theory[1]. Approximation theory attempts to provide an optimal solution to approximating a continuous multivariate function $f(\mathbf{x})$, with an *approximating function* $\hat{f}(\mathbf{w}, \mathbf{x})$, where \mathbf{x} is a N dimensional input vector and \mathbf{w} is a parameter vector used to minimize the approximation error. The set of M input vectors comprise the training set on which the desired input-output mapping, $\{\mathbf{x}_i \rightarrow f(\mathbf{x}_i); i = 1, \dots, M\}$, is defined.

The RBF approximation scheme arises from making certain symmetry assumptions about the smoothing constraints utilized in the regularized solution and corresponds to an approximating function of the form

$$\hat{f}(\mathbf{w}, \mathbf{x}) = \sum_{i=1}^M a_i \exp\left(\frac{-|\mathbf{x} - \mathbf{t}^i|^2}{\sigma_i^2}\right), \quad (2.1)$$

where $\{\mathbf{t}^i\}$ is a set of center locations, $\{\sigma_i\}$ are the corresponding center widths, and $\{a_i\}$ are a set of weighting factors. These three sets define the parameters of \mathbf{w} .

The approximation function given above can be represented in the form of a one layer neural network as shown in Figure 2.1. The hidden layer RBF node response is given by

$$y_i = \exp\left(\frac{-|\mathbf{x} - \mathbf{t}^i|^2}{\sigma_i^2}\right), \quad (2.2)$$

where \mathbf{t}^i is the neuron center and σ_i is the neuron width. The first layer requires the calculation

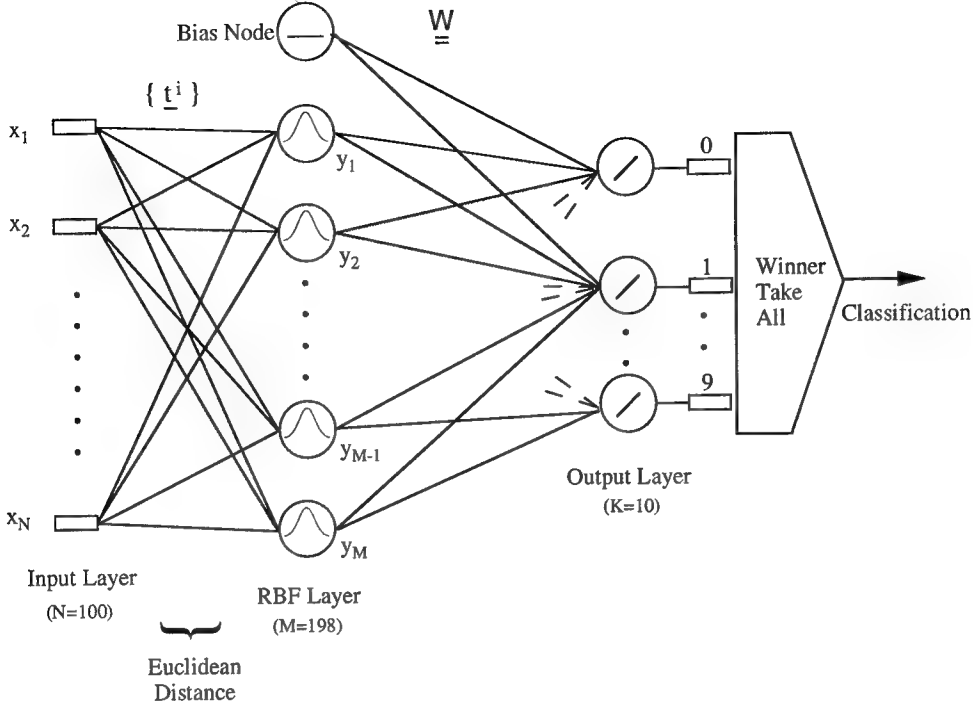


Figure 2.1: Schematic diagram of RBF neural network for digit recognition.

of a Euclidean distance in contrast to conventional networks which use inner products. Also, the neuron response is not sigmoidal but corresponds to a $e^{(-x^2/\sigma^2)}$ function. For a multiple output RBF network the k^{th} output node response to an input vector \mathbf{x} is given by:

$$f_k(\mathbf{x}) = \sum_{i=1}^M a_{ik} \exp\left(\frac{-|\mathbf{x} - \mathbf{t}^i|^2}{\sigma_i^2}\right), \quad (2.3)$$

where a_{ik} is the connection weight between the i^{th} RBF node and the k^{th} output node.

The learning problem for multiple output RBF networks will involve determining $\{\mathbf{t}^i\}$, $\{\sigma_i\}$, and $\{a_{ik}\}$. For our networks the learning is performed in two stages. The first stage involves finding a suitable set of RBF center locations, $\{\mathbf{t}^i\}$. A simple method for choosing RBF center locations is to assign a RBF node for every training point; however, this approach can result in unacceptably large networks. We can improve the first layer hardware efficiency by applying a clustering technique to reduce the number of RBF centers. Although iterative on-line moving centers training algorithms exist[1], we chose to perform training data clustering as a preprocessing step to 'fix' the center locations in order to take advantage of high-contrast static spatial light modulators (SLMs). From a hardware system standpoint the static centers are also much easier to implement since no error feedback to the SLM is required. We use a class-based clustering algorithm[16] to merge nearby in-class training samples into a single center to form prototypes of the training set and to eliminate redundant center locations. The algorithm will merge two same-class training clusters if the criterion, $D_{out} > \alpha R_{in}$ is met, where D_{out} is the distance from the new

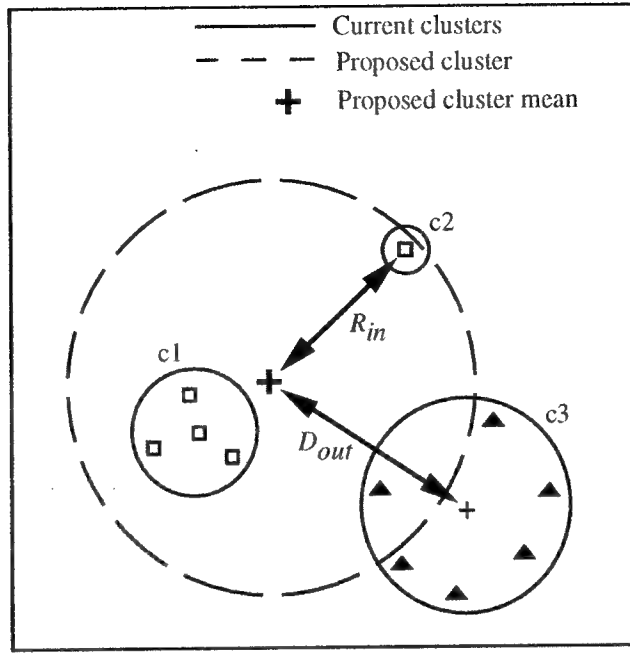


Figure 2.2: Illustration indicating the operation of the class-based clustering technique used to reduce the number of RBF center locations.

cluster mean to the nearest out-of-class cluster mean, α is the ‘clustering parameter’, and R_{in} is the distance from the new cluster mean to the furthest member of the cluster. This is illustrated for the 2D case in Figure 2.2 where the merging of the clusters c_1 and c_2 is considered and c_3 is an out-of-class cluster. Initially all of the training samples form separate clusters and the merging criterion is then applied repeatedly until all possible cluster merges have been considered. The clustering parameter α , controls the extent of overlap between neighboring clusters of differing classes. As α is decreased the overlap between out-of-class clusters is increased and we expect to see a reduction in network classification performance due to reduced class separability. Table 2.1 shows the results of the clustering algorithm applied to a 600 sample training data set, the details of which are described in the next section.

Clustering parameter α	Number of clusters (600 training samples)
3.0	407
2.5	341
2.0	269
1.5	198
1.0	106

Table 2.1: Results of clustering algorithm.

The $\{\sigma_i\}$ and $\{a_{ik}\}$ parameters can be trained by minimizing the squared error at each output node using a gradient descent technique. The squared error of the k^{th} output node in the presence of the single input vector \mathbf{x}^l is defined as

$$(E_k^l)^2 = [\hat{f}_k(\mathbf{w}, \mathbf{x}^l) - f_k(\mathbf{x}^l)]^2.$$

The gradient descent update equation for the p^{th} RBF width is

$$\Delta \left(\frac{1}{\sigma_p^2} \right) = -\alpha_\sigma (E_k^l)^2 (|\mathbf{x}^l - \mathbf{t}^p|^2) a_p \exp \left(\frac{-|\mathbf{x}^l - \mathbf{t}^p|^2}{\sigma_p^2} \right), \quad (2.4)$$

where α_σ is the acceleration constant for the width update. The update equation for the interconnection weight between the p^{th} RBF node and the k^{th} output node is

$$\Delta (a_{pk}) = \alpha_a (E_k^l)^2 \exp \left(\frac{-|\mathbf{x}^l - \mathbf{t}^p|^2}{\sigma_p^2} \right), \quad (2.5)$$

where α_a is the acceleration constant for the weight update. The iterative update equations are applied after each training input vector is presented.

2.2 Handwritten Digit Recognition

Handwritten digit recognition is used to evaluate the performance of our RBF neural network classifier. RBF classifiers have been reported with shorter training times and superior classification performance than either backpropagation networks or k nearest-neighbor classifiers for this problem[8]. Handwritten digit recognition can be viewed as a multi-dimensional classification problem having an output class for each of the ten digits.

We obtained a database of 900 binary, segmented handwritten digits. 600 of the digits are used as the training set and the remaining 300 digits are reserved as a testing set. The input sampling region for each digit is a 40×40 pixel area and examples of the training set are shown in Figure 2.3. The RBF network is not inherently scale, position, or rotation invariant although by providing enough training data for these distortions new centers can be formed for each distorted view[2]. A more efficient approach however, is to preprocess the digits in a class independent manner by centering and scaling them to minimize position and scale variation. From the 40×40 pixel image the maximum extent of each digit is found and the digit is scaled and centered into a new 10×10 pixel image (see Figure 2.4). The 10×10 pixel image is then unrastered to form a 100 bit *binary* vector used as input to the RBF classifier. In practice character recognition systems may use more sophisticated feature-extraction methods in order to further improve both efficiency and discrimination ability[17]. This data preprocessing must be performed before the training set clustering algorithm described in the previous section can be applied. From the training set clustering results presented in Table 2.1 we chose to use 198 cluster centers each of 100 bit length for our optical system since commercial SLMs of this resolution (i.e. 100×200) are readily available.

To illustrate the capabilities of the RBF neural network in the application of handwritten digit recognition we train and test a software version of the network described above. The training set

0	0	0	0	0	0	0	0	0	0
1	1	1	1	1	1	1	1	1	1
2	2	2	2	2	2	2	2	2	2
3	3	3	3	3	3	3	3	3	3
4	4	4	4	4	4	4	4	4	4
5	5	5	5	5	5	5	5	5	5
6	6	6	6	6	6	6	6	6	6
7	7	7	7	7	7	7	7	7	7
8	8	8	8	8	8	8	8	8	8
9	9	9	9	9	9	9	9	9	9

Figure 2.3: Samples of unprocessed 40x40 pixel digits.

0	0	0	0	0	0	0	0	0	0
1	1	1	1	1	1	1	1	1	1
2	2	2	2	2	2	2	2	2	2
3	3	3	3	3	3	3	3	3	3
4	4	4	4	4	4	4	4	4	4
5	5	5	5	5	5	5	5	5	5
6	6	6	6	6	6	6	6	6	6
7	7	7	7	7	7	7	7	7	7
8	8	8	8	8	8	8	8	8	8
9	9	9	9	9	9	9	9	9	9

Figure 2.4: Samples of centered and scaled 10x10 pixel digits.

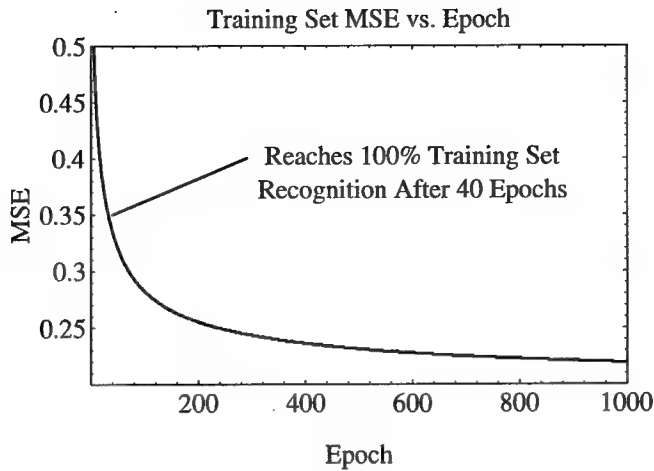


Figure 2.5: Training history of software RBF neural network error.

inputs are presented sequentially to the network. The error at each output node is calculated and the update equations are applied to iteratively minimize the network errors. The mean squared error (MSE) measure is used to evaluate the system performance as the network trains. The MSE is given by

$$MSE = 1/P \sum_{l=1}^P \left(\sum_{j=1}^K (E_j^l)^2 \right),$$

where $P = 600$ is the number of training set samples and $K = 10$ is the number of output nodes. Figure 2.5 shows the MSE of the network during training for the first 1000 epochs (training cycles). The best results obtained were 100.0% recognition of the training set and 97.7% correct recognition of the testing set data. These recognition rates serve as a baseline for comparing the performance of the software RBF neural network with the optical hardware neural network that we present in the following chapters.

3

OPTICAL RBF NEURAL NETWORK

In this chapter we describe an opto-electronic implementation of the parallel RBF neural network classifier[15]. The hardware implementation of the RBF classifier is composed of two subsystems, the first is a parallel Euclidean distance computer which we implement in optics. This subsystem is spatially multiplexed, making use of two-dimensional SLMs to represent the center locations. The second subsystem evaluates the basis functions and performs the interconnect weighting between the RBF layer and the output layer. An analog electronic hardware design is proposed for implementing the postprocessing subsystem. In our system the optically computed distances are captured with a CCD camera and the postprocessor is simulated in software.

3.1 Parallel Optical Distance Computation

The first layer of the RBF neural network computes the Euclidean distance between the input and each of the centers. The Euclidean distances $\{d^i\}$, between a vector \mathbf{x} , and the centers $\{\mathbf{t}^i\}$, can be written as

$$d^i = |\mathbf{x} - \mathbf{t}^i|^2 = \sum_{j=1}^N (x_j - t_j^i)^2 = \sum_{j=1}^N d_j^i, \quad (3.1)$$

where

$$\overline{d_j^i} = x_j t_j^i + \overline{x_j} \overline{t_j^i}, \quad (3.2)$$

for the case of binary vectors. The overbar indicates a bitwise complement. We can implement this distance computation in parallel hardware using the optical system shown in Figure 3.1. A photograph of the system fabricated in-house is shown in Figure 3.2. This system is spatially multiplexed in contrast to previously demonstrated time multiplexed optical disk-based systems[15, 18]. The light in *LEG 1* of the system illuminates the input SLM labeled \mathbf{x} and is then collimated in the y direction and imaged in the x direction onto the centers SLM labeled t_j^i . The result that appears immediately behind the centers SLM is the product term $\{x_j t_j^i ; i = 1, \dots, M; j = 1, \dots, N\}$, which is required in the distance computation. *LEG 2* of the system forms the products

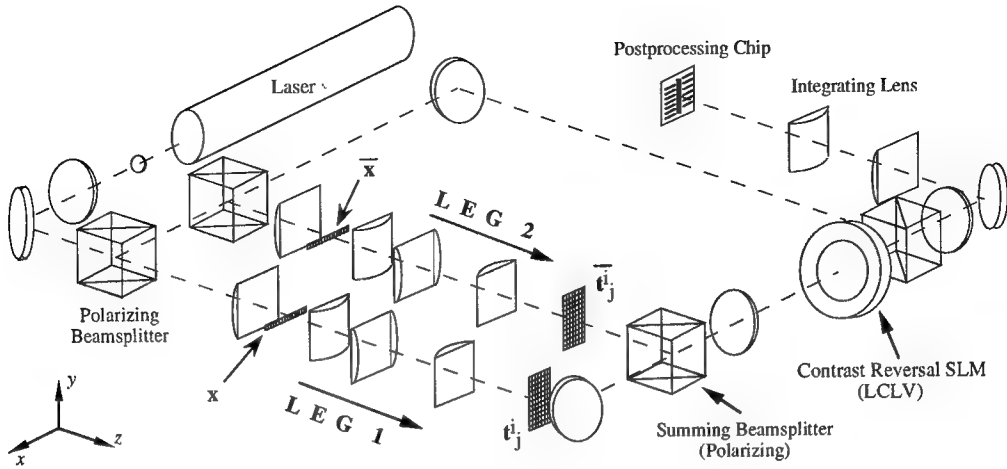


Figure 3.1: Dual-rail vector-matrix multiplier used as a parallel optical distance computer.

$\{\bar{x}_j \bar{t}_j\}$ in a similar fashion. The results of these vector-matrix multipliers are simultaneously imaged onto a contrast-reversing liquid-crystal light valve (LCLV) SLM where they are superimposed to form the terms $\{\bar{d}_j^i\}$. The result of the contrast reversal yields the $\{d_j^i\}$ terms and the final integration operation $\sum_{j=1}^N d_j^i$, is performed using a cylindrical lens.

We implement the standard RBF neural network paradigm which does not incorporate a moving centers algorithm[1]. This allows the center locations to be placed upon fixed masks such as etched chrome or developed film on glass for high contrast and uniformity over the entire mask area. In our system the centers masks are film negatives. Figure 3.3 shows a sample centers mask with 198, 100-dimensional center locations. All of the centers belonging to a class are placed together in order to minimize the effects of crosstalk between classes. Additionally, a blank spacer vector (not shown) is placed between classes to prevent inter-class crosstalk. The pixel size used for the centers masks is $63.5 \mu m$ center-to-center. The overall centers mask area is approximately 1.0 cm by 2.0 cm . Additional vectors are placed on either side of the centers data vectors to aid in alignment and data normalization. In this system the input vectors are also placed onto film since the training and testing sets were fixed. For real-time operation electronically-addressed 1D SLMs would be used for the \mathbf{x} and $\bar{\mathbf{x}}$ inputs.

Figure 3.1 shows the actual (a) and optically computed distances (b) between an input vector representing the digit '0' and the 198 center locations (templates). As a comparison Figure 3.4 shows the corresponding distances for the input digit '4'. Although large errors are present in the optically computed distances we observe that the distances are generally smallest for the appropriate template numbers. The accuracy of the optical distance computation can be quantified using the formula

$$\Delta D_{rms} = \frac{\left[1/M \sum_{i=1}^M (d_i^{Opt} - d_i^{Act})^2 \right]^{1/2}}{1/M \sum_{i=1}^M d_i^{Act}}, \quad (3.3)$$

where d_i^{Opt} are the Euclidean distances between the 300 testing inputs and the 198 centers calculated from the optical system and d_i^{Act} are the actual Euclidean distances. The average rms distance

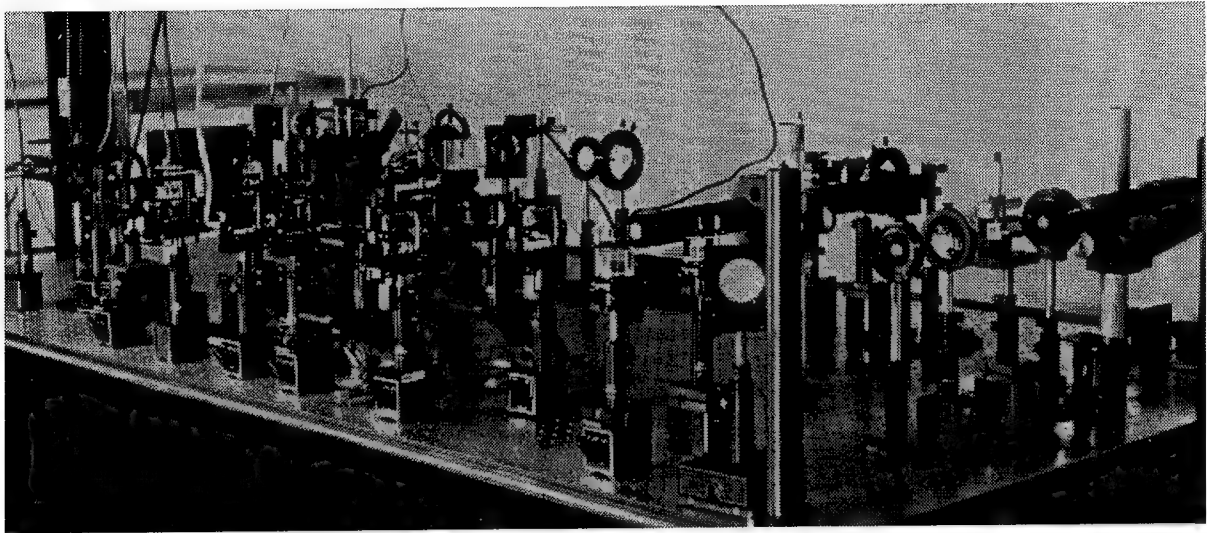


Figure 3.2: Picture of optical RBF classifier system.

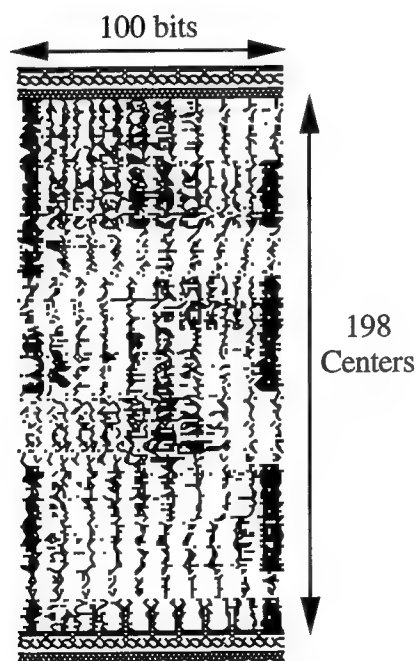


Figure 3.3: Example of a centers mask (not to scale).

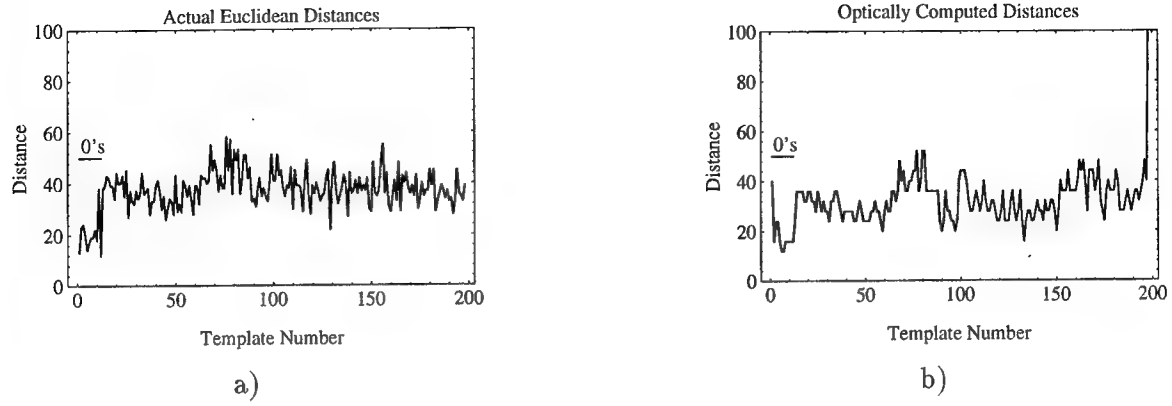


Figure 3.4: Euclidean distance vs. template number for a single input image (handwritten 0).
a) Actual distance and b) optically computed distance.

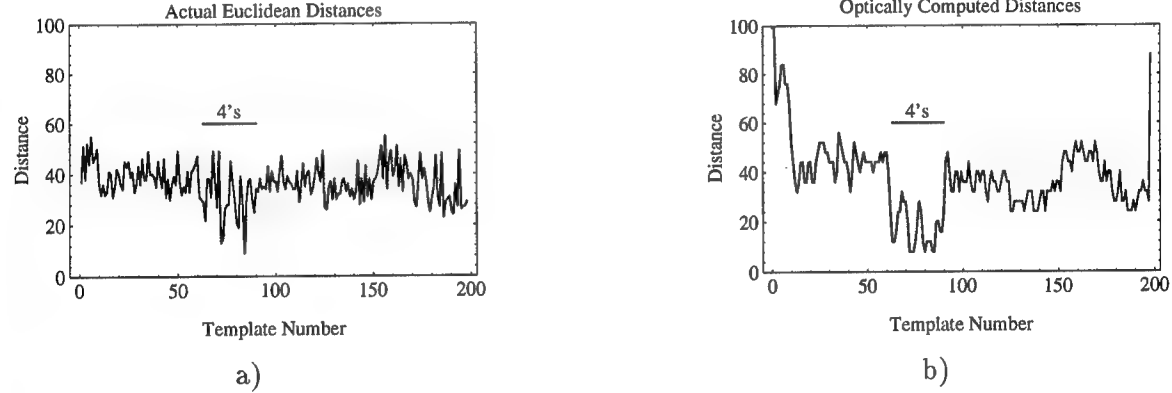


Figure 3.5: Euclidean distance vs. template number for a single input image (handwritten 4).
a) Actual distance and b) optically computed distance.

error over the testing set for our optical system is measured to be 29%. This large 29% distance computation error result will lead to a large classification error in our system. The errors present in the optical distance computation are due to device imperfections and system noise that will be discussed in the next chapter.

3.2 Parallel Basis Function Evaluation

We now consider the second subsystem of the RBF classifier which performs the basis function evaluation and output interconnect weighting. The block diagram in Figure 3.6 shows a possible analog electronic implementation of the subsystem for the single output case[15]. Each array of 198 modules provides a single network output; therefore, we require ten such arrays for our application. Note that all of the proposed operations are local with exception of the global sum and are compactly

Class	Optical	Software
	(Correct out of 30)	
0	0	29
1	0	30
2	0	28
3	4	29
4	30	29
5	28	28
6	5	30
7	26	30
8	0	30
9	0	30
Total	93	293
Overall recognition	31.0%	97.7%

Table 3.1: Performance comparison between optical RBF classifier and software RBF classifier.

achievable in analog VLSI circuitry. In this non-adaptive postprocessor the network center widths and interconnection weights can be trained ‘off-line’ in software and then downloaded to the chip during operation. In our experiments the analog postprocessor chip is emulated in software.

A software RBF neural network was trained using the preprocessed training data. The center widths and interconnect weights are taken from the trained network and loaded into the software postprocessor emulator. Then using the optically computed distances of the test set we evaluated the optical neural network classifier performance. The overall recognition rate for the RBF classifier is 31.0%. This very poor performance does not agree with the 97.7% testing recognition rate measured from the RBF network software simulations presented in Section 2.2. A class-wise comparison between the performances of the RBF network using the optically computed distances and the perfectly computed distances is shown in Table 3.1. It is evident that the distance errors caused by the optical system imperfections have a catastrophic effect upon the overall system performance. Although it may be possible to use a detailed model of the optical system to more accurately compute the center widths and interconnect weights, the measurement of system parameters would be difficult to make for highly integrated, compact systems. More importantly, temporal changes in the system can greatly effect the system operation. Therefore it is highly desirable to perform on-line adaptation of the network parameters.

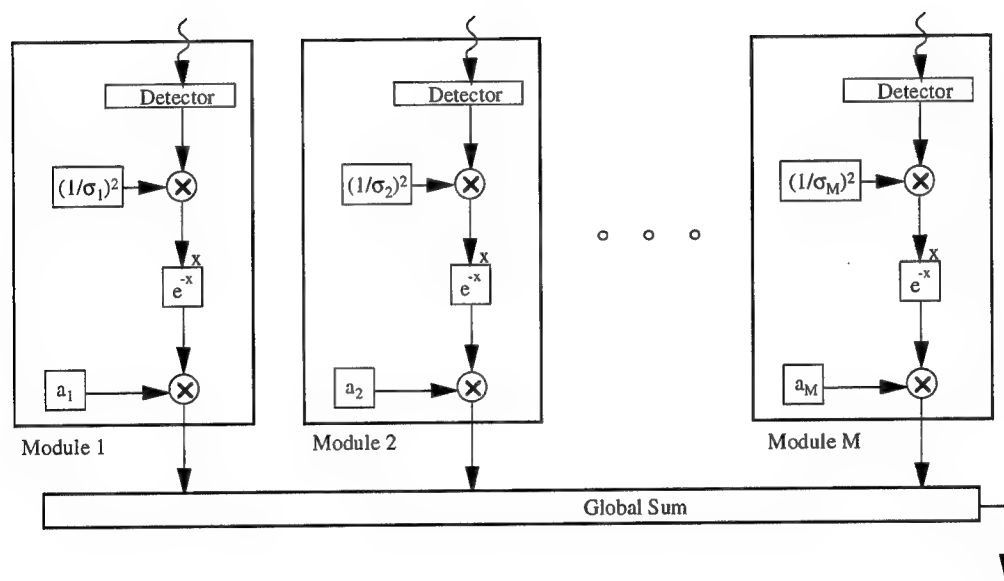


Figure 3.6: Non-adaptive RBF postprocessing chip for a single output network.

4

NOISE CHARACTERIZATION AND COMPUTER MODELING

We now present a noise analysis of the optical RBF system. This analysis will help to identify the limiting noise sources that lead to the large decrease in performance of the optical system as compared to the software RBF neural network. To better understand the effects of each noise term on the overall system performance we have developed a detailed computer model of the optical system which uses parameters taken from the actual optical hardware. The noise terms that are incorporated in the model include:

1. optical system imperfections (illumination nonuniformities, input and centers SLM finite contrast, and optical system PSF),
2. LCLV response (intensity transfer function, spatial resolution, and fixed-pattern noise),
3. detector response (A/D quantization error and detector random noise).

The following sections present the mathematical expressions used to represent each of these noise terms in our computer model. Each noise term is characterized in terms of its effect upon the optical distance computation as given in Equations (3.1) and (3.2).

4.1 Optical System Noise Characteristics

4.1.1 Illumination Characteristics

There are two different Gaussian laser beam profiles present in each vector-matrix multiplier. This is due to the cylindrical optics which performs collimation along one axis and imaging in the other. The resulting anamorphic beam profile can be measured directly behind the plane of the centers mask SLM. The effect upon the distances can be expressed as

$$\hat{d}_j^i = [G_1(j, i)x_j t_j^i] + [G_1(j, i)\bar{x}_j \bar{t}_j^i],$$

where

$$G_1(j, i) = \exp \left(- \left(\frac{(j - j_0)}{\sigma_1} \right)^2 - \left(\frac{(i - i_0)}{\sigma_2} \right)^2 \right),$$

and \hat{d}_j^i is the optically generated estimate of \overline{d}_j^i , and (j_0, i_0) represents the midpoint of the centers SLM array. The imaging axis profile σ_1 , is along the length of the 1D input SLM. The collimating axis beam profile σ_2 , is proportional to the beam expansion in the vector-matrix multiplier and is orthogonal to σ_1 . The beam profiles can be calculated from the beam intensity at the edge of the SLM using the formula:

$$\sigma = \sqrt{\left(\frac{-D^2}{2 \ln(E)} \right)},$$

where D is the distance from the edge of the SLM to the center of the SLM, and E is the ratio of the beam intensity at the SLM edge to the beam intensity at the center of the SLM. In the LCLV read-out portion of the system there is another Gaussian beam profile (circular) which corrupts the distance computation according to

$$\hat{d}^i = \sum_{j=1}^N G_2(j, i) d_j^i,$$

where

$$G_2(j, i) = \exp \left(- \left(\frac{(j - j_0) + (i - i_0)}{\sigma_3} \right)^2 \right),$$

and \hat{d}^i is the optically generated estimate of d^i .

4.1.2 SLM Characteristics

In our system we made use of film negatives to act as SLMs for both the center locations and the input vectors. By employing film masks we can achieve very high contrast ($> 100:1$) and uniformity over the entire mask. While it may be realistic to use these static SLMs for the center locations in a dedicated real-time optical processor, an electronically-addressable SLM would generally be required for the input vector SLMs. Electronically-addressed SLMs typically have contrast ratios in the range of 10:1 to 100:1. The effect of finite contrast SLMs on the distance computation can be represented by

$$\hat{d}_j^i = \left[x_j + \left(\frac{1 - x_j}{C_r} \right) \right] \left[t_j^i + \left(\frac{1 - t_j^i}{C_r} \right) \right] + \left[\overline{x}_j + \left(\frac{1 - \overline{x}_j}{C_r} \right) \right] \left[\overline{t}_j^i + \left(\frac{1 - \overline{t}_j^i}{C_r} \right) \right],$$

where C_r is the contrast ratio.

4.1.3 LCLV Characteristics

The device used to perform contrast reversal in our system is a Hughes LCLV (pre-1987). In our experiment the contrast, uniformity, and resolution were critical characteristics for the LCLV device. The contrast is determined by the transfer function of the device. The intensity transfer function of our contrast-reversing LCLV is shown in Figure 4.1 along with the response curve used

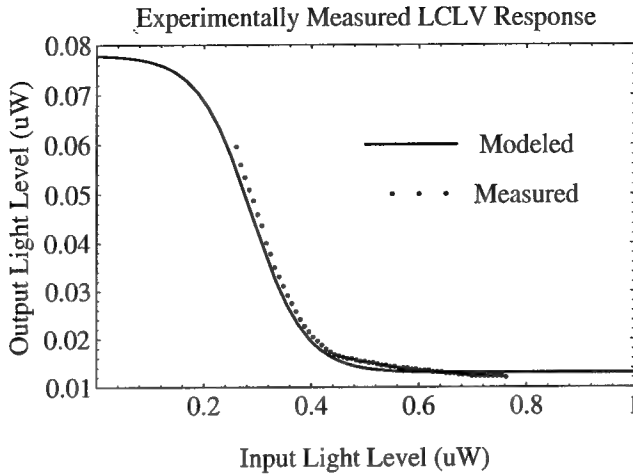


Figure 4.1: Measured and modeled LCLV transfer functions.

in the computer model. The effect of the LCLV response on the optical distance computation can be represented as

$$\hat{d}^i = \sum_{j=1}^N TF(\bar{d}_j^i),$$

where TF is the transfer function

$$TF(I) = \theta_o - \alpha \left(\frac{1}{1 + \exp \left(\frac{-I + \theta_i}{\gamma} \right)} \right).$$

In this expression for the LCLV transfer function I represents the input intensity, θ_i is the intensity bias of the input illumination, θ_o is the bias of the output (read-out) intensity, α is an output scaling factor, and γ is the slope of the transfer curve.

One of the largest errors in our system arises from fluctuation of the LCLV transfer function over time. We have measured these variations in LCLV transfer function and Figure 4.2 is a representative example of read-side intensity versus time for a fixed write-side intensity. Figure 4.2 shows a temporal variation of nearly 20% of the entire intensity range for a single pixel (approximately $50 \mu\text{m}^2$ area of the LCLV). We observed that the ‘dark’ regions on the read-side of the LCLV have a greater temporal variation than the ‘bright’ regions. This is because the ‘dark’ regions on the read-side of the contrast-reversing LCLV correspond to bright illumination on the write-side. Measurements taken on the write-side of the LCLV indicate that the LCLV device is the source of the temporal fluctuations, not the laser. This presents a difficult error for the system to adapt to since our system’s distance computations critically depend on the ‘darker’ areas which define the smallest distances. Due to non-uniformities in our LCLV certain portions of the device appear to fluctuate more than others. Heat external to the device is thought to be the primary cause of these fluctuations. The data presented in this paper was taken during periods when the these temperature induced fluctuations were at a minimum. This problem can be tolerated in a real-time system by periodically calibrating the system. Alternatively, there are other newer commercial devices available which have superior performance characteristics[19].

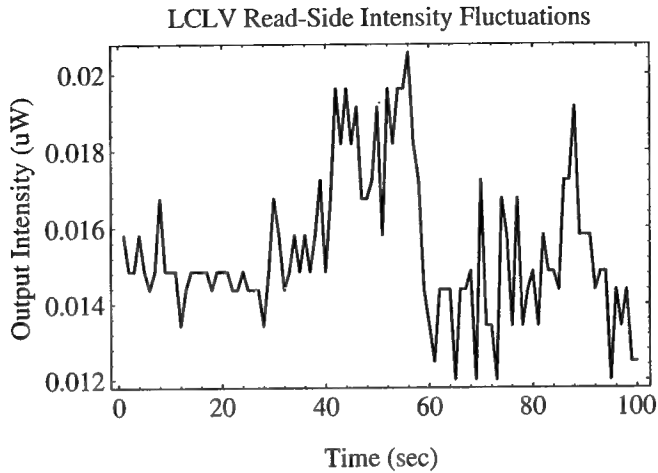


Figure 4.2: Measured intensity fluctuations over time measured on a $50 \mu\text{m}^2$ area of the LCLV.

4.1.4 System Noise Characteristics

The effects of random detector noise on the optical distance computations can simply be represented by

$$\hat{d}^i = \sum_{j=1}^N (d_j^i + \eta_d),$$

where η_d is a random variable with a Gaussian distribution. The detector noise is modeled as stationary additive noise and is a result of detector dark current. The noise variance was assumed to be on the order of 2% of the detector's full scale range[20]. The A/D quantization error also effects the distance computation. This noise source can be represented as

$$\hat{d}^i = \sum_{j=1}^N (d_j^i / d_{j_{max}}^i) (2^{n \text{ bits}}),$$

where $2^{n \text{ bits}}$ is the number of quantization levels in the A/D conversion. Eight bit quantization was used in our optical RBF system.

4.1.5 Other Optical System Characteristics

Two other important error sources impacting our optical distance measurements are the LCLV resolution limit and the ratio of light intensity between the two legs in the optical distance computer. We measured our LCLV resolution to be 8.0 lines/mm using the Air Force resolution target. The pixel pitch in our centers masks is $63.5 \mu\text{m}$ which requires a minimum resolution of 15.8 lines/mm at a $1.0 \times$ magnification. The LCLV aperture is 50.0 mm in diameter which allows us to image the centers masks onto the LCLV at an increased magnification. The factor that limits this magnification is nonuniformity in the active area of the LCLV. Figure 4.3 is a picture showing nonuniformities in the area surrounding the centers mask image as viewed from the read-side of the LCLV. The

Parameter	Measured Values
Nonuniform Illumination	
Imaging Axis, σ_1	0.28
Collimating Axis, σ_2	0.13
Read-out Beam, σ_3	0.32
SLM Finite Contrast, C_r	> 100:1
Leg Intensity Ratio, β_1/β_2	0.96
LCLV Blur, σ_b	0.85
LCLV Transfer Function, $\theta_i, \theta_o, \alpha, \gamma$	0.29, 0.078, 0.065, 0.05
Detector Noise, σ_d	0.02
A/D Quantization, $2^{n \text{ bits}}$	8 bits

Table 4.1: Measured error values from optical system.

nonuniformities are thought to be caused by liquid crystal thickness variations, fringes from the LCLV readout cover glass, and spherical curvature due to imperfect photoconductor flatness [21]. The magnification in our system was increased to nearly $1.5\times$ to make the best use of a uniform area of the LCLV. The LCLV resolution limit and optical system PSF are modeled together as a Gaussian blur that impacts the optical distance computation according to

$$\hat{d}_j^i = h(i, j) * (x_j t_j^i + \bar{x_j} \bar{t}_j^i),$$

where the $*$ symbol denotes a convolution and $h(i, j)$ is an $n \times n$ Gaussian convolution kernel. In our system the Gaussian kernel width is measured to be $\sigma_b = 0.85$ pixels of the centers SLM (labeled t_j^i in Figure 3.1) which can be adequately modeled with a 3×3 pixel kernel.

The second optical system error is the beam intensity ratio between *LEGS 1* and *2* shown in Figure 3.1. The impact of this light intensity ratio on the optical distance computation can be expressed as

$$\hat{d}_j^i = \beta_1(x_j t_j^i) + \beta_2(\bar{x_j} \bar{t}_j^i),$$

where β_1/β_2 is the leg intensity ratio. We make use of a polarizing beam-splitter to direct orthogonally polarized light into each of the two legs in order to minimize interference fringes at the summing beam-splitter. Placing a wave plate before the polarizing beam-splitter allows us to adjust the leg intensity ratio by rotating the wave plate.

4.2 Optical System Software Model

Using our computer model of the optical system together with the measured system noise parameters shown in Table 4.1 we generate a set of simulated optical testing set distances. As in the last chapter we again use the center widths and interconnect weights computed off-line from the software RBF neural network to test the system, this time using the simulated optical distances instead of the actual optical distances. Our testing recognition result is 29.0% which agrees well



Figure 4.3: Image of the readout side of the LCLV depicting nonuniformities (slightly out of focus).

Class	Optical	Model
	(Correct out of 30)	
0	0	0
1	0	0
2	0	0
3	4	1
4	30	30
5	28	28
6	5	2
7	26	26
8	0	0
9	0	0
Total	93	87
Overall recognition	31.0%	29.0%

Table 4.2: Performance comparison between optical RBF classifier and modeled optical RBF classifier.

with the recognition rate of 31.0% obtained with the actual optically computed data. The class-wise performance comparison between the model predictions and the optical system is shown in Table 4.2. This result suggests that we can now accurately predict the system performance of our optical hardware RBF neural network using our computer model. Furthermore, the model allows us to simulate other system operating points from which we can deduce which noise terms are most critical for the overall system performance. These issues will be pursued further in the next chapter.

5

ADAPTIVE OPTICAL RBF NEURAL NETWORK

As we have seen in the last two chapters our optical hardware network performance greatly suffers due to errors in distance computation caused by optical system imperfections and noise. We expect that by training our optical system in the presence of these imperfections, the network will compensate for these errors and its performance will more closely match that of the software RBF network. In this chapter we consider an adaptive postprocessor[15] and present computer model comparisons between adaptive and non-adaptive RBF classifier systems.

5.1 Adaptive Postprocessor

By modifying the non-adaptive single-output postprocessor chip design presented in Section 3.2 we can incorporate error feedback in order to implement on-line network training. Using the electronic module shown in Figure 5.1 we can directly implement the gradient descent update Equations (2.4) and (2.5). In addition to error feedback for each module we also require accumulation registers for adapting both the RBF widths and weights in an iterative fashion. As in the non-adaptive case we need to have ten arrays, each consisting of 198 modules for the optical fully-parallel implementation of the digit recognition RBF network shown in Figure 2.1.

5.2 Influences of Noise on System Performance

Using a computer model of the optical Euclidean distance computation subsystem and its ability to include the effects of optical system error sources, we have studied the effects of these errors on the optical RBF system's recognition performance. Optical systems that use adaptive or "on-line" training to compensate for these errors can be compared with optical systems that are trained "off-line" in order to estimate the utility of adaptive training in this application. We now present computer model performance comparisons between the adaptive and non-adaptive hardware

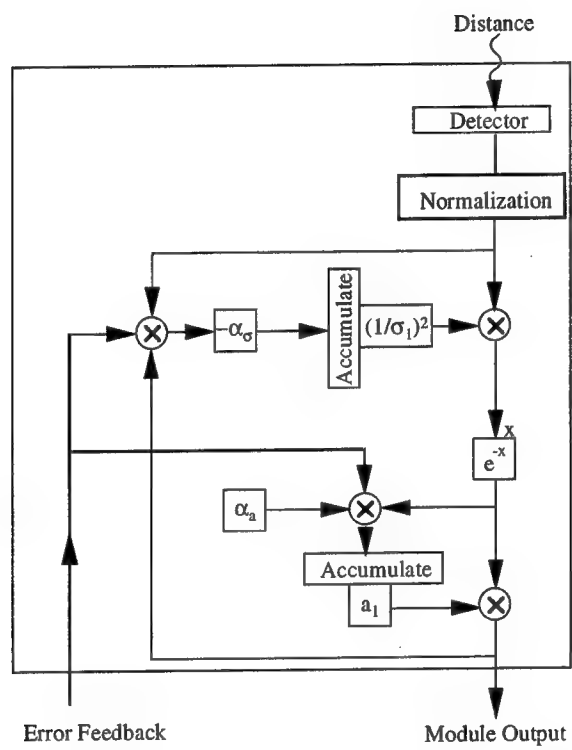


Figure 5.1: Adaptive RBF postprocessing chip module.

systems. Two performance plots are provided for each of the error sources found to be most critical in our system. The first plot assumes the optical system to be ideal (error free) except for the error under consideration. The second plot predicts the influence of the error given all other parameters are fixed at their values as measured from the optical system and as shown in Table 4.1. Each plot shows two performance curves, the solid line indicates the system testing performance when trained in the presence of the imperfection (adaptive on-line training) and the dashed line shows the testing results when trained off-line as in the non-adaptive case. The measured system operating points are indicated in each plot by a vertical line.

Figure 5.2 shows the predicted system testing recognition rate as a function of the imaging axis beam profile and Figure 5.3 shows the result for the collimating axis case. As expected the performance in both cases degrades with an increasingly nonuniform beam profile. It can also be observed that the 'on-line' training significantly improves the performance as compared to the 'off-line' training. Although the imaging axis error effects all of the centers by the same degree it will reduce a portion of the system's discrimination ability if the pixels on the edge of the SLM are not of sufficient intensity to transmit through the LCLV. The effect of the collimating beam error has more influence on system performance since it effects each center location vector to a different degree. It can be shown that the digit classes with centers near the outer edges of the SLM are more likely to be misclassified (e.g. see Table 3.1), attesting to the spatial dependence of the centers. While it may be possible to use this *a priori* information to design a more robust sequence of the centers, it is more desirable to correct the beam profile using increased beam-expansion, diffractive optic elements, or holograms. The predicted system performance in the presence of only the LCLV read-out beam profile is shown in Figure 5.4. The read-out profile is shown to have little impact on the system performance.

Figure 5.5 shows the predicted system testing recognition rate versus finite SLM contrast. The system performance does not degrade appreciably until the SLM contrast C_r , falls below 10. This differs from the results of previous systems[15] in which finite SLM contrast was found to be a dominant error source.

The predicted results of the leg intensity ratio are presented in Figure 5.6. It is interesting to note that in the ideal system case shown in Figure 5.6a the adaptive training fails to outperform the non-adaptive system.

5.3 Adaptive Optical RBF Neural Network Results

We now use the adaptive system model and the measured noise parameter values from the experimental optical system in Table 4.1 to make predictions about the adaptive system performance. The model predicts an overall testing recognition rate of 94.7% when trained on-line. Using the actual optically computed testing distances together with the on-line learning gives a final recognition rate of 92.67%. Table 5.1 shows the class-wise recognition performance corresponding to these results. Using a confusion matrix we can analyze the network misclassifications of the testing set data. Table 5.2 presents the confusion matrix for the actual adaptive optical network. We observe that the '2's are misclassified as '3's and '6's and the '5's are misclassified as '8's and '3's. These results suggest that adding more centers to the classes of '2's and '5's may improve the network's classification abilities. Again the model is in good agreement with the experimental system performance

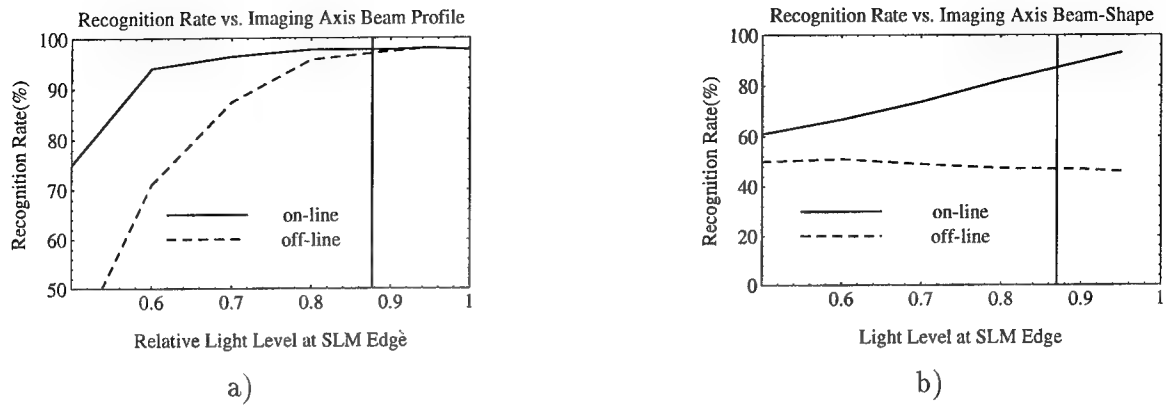


Figure 5.2: Predicted recognition rate versus imaging axis beam profile. a) Otherwise ideal system. b) Incorporating all error sources.

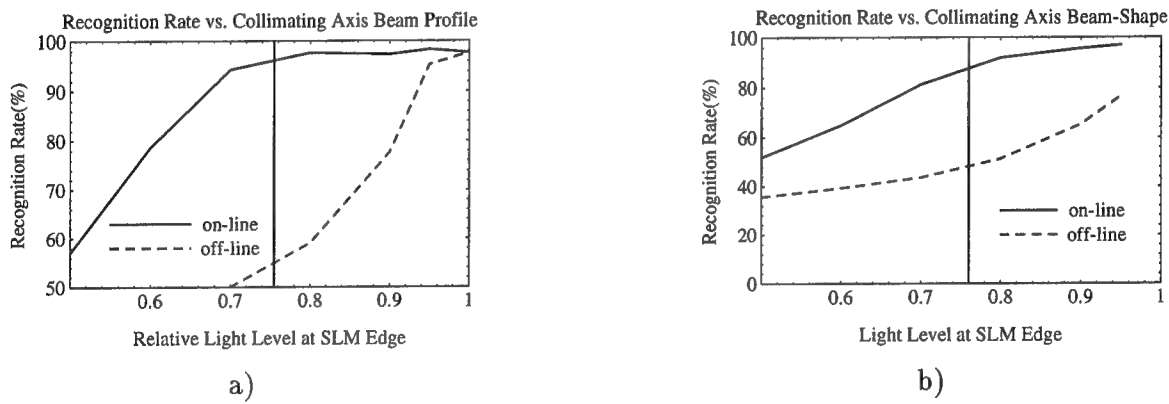


Figure 5.3: Predicted recognition rate versus collimating axis beam profile. a) Otherwise ideal system. b) Incorporating all error sources.

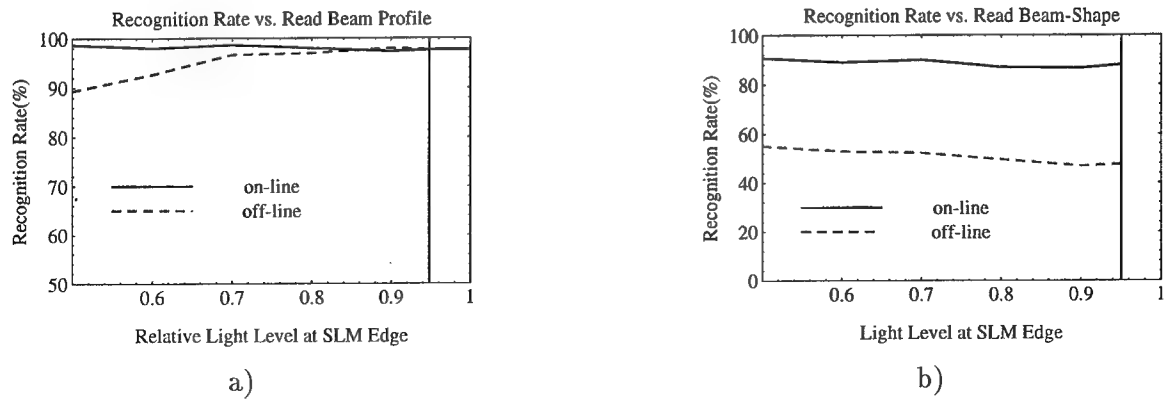


Figure 5.4: Predicted recognition rate versus LCLV readbeam profile. a) Otherwise ideal system. b) Incorporating all error sources.

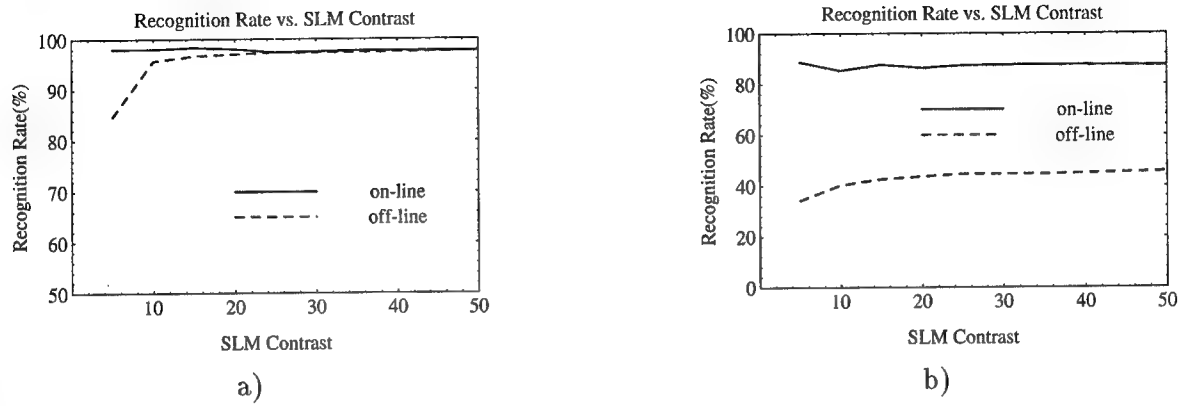


Figure 5.5: Predicted recognition rate versus finite SLM contrast. a) Otherwise ideal system.
b) Incorporating all error sources.

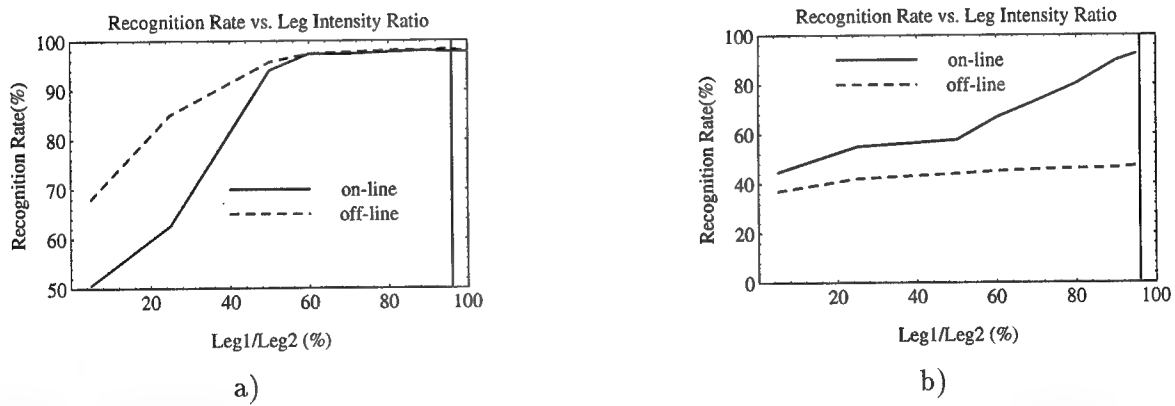


Figure 5.6: Predicted recognition rate versus leg intensity ratio. a) Otherwise ideal system. b) Incorporating all error sources.

Class	Optical	Model
	(Correct out of 30)	
0	30	29
1	30	30
2	22	23
3	28	28
4	30	30
5	21	26
6	27	28
7	30	30
8	30	30
9	30	30
Total	278	284
Overall recognition	92.67%	94.67%

Table 5.1: Performance comparison between adaptive optical RBF classifier and the modeled adaptive optical RBF classifier.

illustrating the utility of the computer model predictions. The adaptive optical system provides us with nearly 60% increase in recognition performance as compared to the non-adaptive optical RBF classifier, attesting to the significant improvement imparted by adaptive on-line training.

Input Class	Network Output Classification (Number of outputs in each class)									
	0	1	2	3	4	5	6	7	8	9
0	30	0	0	0	0	0	0	0	0	0
1	0	30	0	0	0	0	0	0	0	0
2	0	0	22	5	0	0	3	0	0	0
3	0	0	0	28	0	1	1	0	0	0
4	0	0	0	0	30	0	0	0	0	0
5	0	0	0	2	0	21	1	0	5	1
6	0	0	0	0	1	0	27	0	2	0
7	0	0	0	0	0	0	0	30	0	0
8	0	0	0	0	0	0	0	0	30	0
9	0	0	0	0	0	0	0	0	0	30

Table 5.2: Confusion matrix for adaptive optical RBF network.

6

CONCLUSIONS AND FUTURE WORK

We have demonstrated a spatially multiplexed parallel optical system capable of implementing a RBF classifier. The system was trained using 600 handwritten digits 0-9, and tested on a disjoint set of 300 digits. The optical system computes the Euclidean distances between a 100 bit input vector and 198 centers in parallel. Our experimental results show that training the RBF network in the presence of optical imperfections and noise versus training the network 'off-line' can improve the testing recognition rate by nearly 60%. When the network is trained 'off-line' and then tested on data from the optical system its recognition rate is 31.0% which agrees well with our computer model's prediction of 29.0%. The testing performance improves considerably when the network is trained 'on-line', using data from the optical system. The experimental recognition rate of 92.67% agrees well with our model's prediction of 94.67% for the adaptive case. In order to implement a real-time system it is necessary to replace the film masks with dynamic SLMs and to design and fabricate an electronic adaptive postprocessor. The primary error source in our system arose from the LCLV used for contrast-reversal. The use of an alternative device is recommended for higher performance and reliability.

One future area of research will be to extend the adaptive optical radial basis function neural network classifier to permit analog and complex-valued input signals. Many signal and image processing applications are best approached by analyzing the inherently complex-valued frequency-domain data. Recent studies have shown that complex-domain neural networks out-perform real-domain neural networks in applications that require the processing of frequency-domain or phase-plane data[22, 13]. One particular application of this proposed complex-input system is radar direction finding.

A new antenna beamforming approach 'neural beamforming', has been developed at Rome Laboratory by researchers Major Jeffrey Simmers and Dr. Hugh Southall of RL/ERAS and Terry O'Donnell from the ARCON Corporation [23, 24, 25, 26]. Their goal is to design neural processing algorithms that can adapt to low cost phased-array antennas, even if the antennas behave in a nonlinear manner, are imperfectly manufactured, or become degraded after some period of time. Neural beamforming techniques can decrease antenna manufacturing and maintenance costs and

increase mission time and performance between repair actions. Their work has focused on signal detection and direction finding for single and multiple sources (targets).

The group has presented two neural beamformers, both based on RBF neural networks. Although other neural network paradigms have been previously considered the RBF approaches provide the best overall performance. Both an adaptive RBF (ARBF) network and a linear algebra RBF (LINNET) network training algorithm have been employed in the beamforming application. Most of their work has centered around the adaptive RBF neural beamformer that uses a training procedure similar to one used for our adaptive optical system. The input to the neural beamformer consists of complex-valued data from the output of a 32 element phased-array antenna. It should be noted that it is desirable to perform that direction finding at MHz data rates and military phased array antennas typically have between 200 and 1000 antenna elements. These data processing rates are not attainable with current or near-term sequential computer hardware systems. The group is now beginning to search for parallel processing hardware in order to meet this signal processing demand. An analog adaptive optical RBF classifier system may present a viable solution to this large, real-time problem.

REFERENCES

- [1] T. Poggio and F. Girosi. Networks for Approximation and Learning. *Proc. of the IEEE*, 78(9):1481–1497, September 1990.
- [2] T. Poggio and S. Edelman. A network that learns to recognize three-dimensional objects. *Nature*, 343:263–266, 18 Jan 1990.
- [3] G. Vrckovnik, C. Carter, and S. Haykin. Radial Basis Function Classification of Impulse Radar Waveforms. In *Proc. of IJCNN*, volume I, pages 45–50, June 1990.
- [4] R. Brunelli and T. Poggio. Face Recognition: Features versus Templates. *IEEE Trans. Patt. Anal. Machine Intell.*, 15(10):1042–1052, 1993.
- [5] N. Arad, N. Dyn, D. Reisfeld, and Y. Yeshurun. Image Warping by Radial Basis Functions: Application to Facial Expressions. *CVGIP*, 56(2):161–172, 1994.
- [6] J. L. Blue, G. T. Candela, P. J. Grother, R. Chellappa, and C. L. Wilson. Evaluation of Pattern Classifiers for Fingerprint and OCR Applications. *Pattern Recognition*, 27(4):485–501, 1994.
- [7] S. Renals and R. Rohwer. Phoneme Classification Experiments Using Radial Basis Functions. In *Proc. of IJCNN*, volume I, pages 461–467, Wash. D.C., June 1989.
- [8] Yuchun Lee. Handwritten Digit Recognition Using K Nearest-Neighbor, Radial Basis Function, and Backpropagation Neural Networks. *Neural Computation*, 3:440–449, 1991.
- [9] M. A. Neifeld, S. Rakshit, and D. Psaltis. Handwritten zip code recognition using an optical radial basis function classifier. In *Proc. of SPIE*, volume 1469, pages 250–255, 1991.
- [10] D. S. Broomhead and D. Lowe. Multivariable Functional Interpolation and Adaptive Networks. *Complex Systems*, 2:321–355, 1988.
- [11] D. S. Broomhead. Signal processing for nonlinear systems. In *Proc. SPIE*, volume 1565, pages 228–243, 1991.
- [12] L. Xu, A. Krzyzak, and A. Yuille. On Radial Basis Function Nets and Kernel Regression: Statistical Consistency, Convergence Rates, and Receptive Field Size. *Neural Networks*, 7(4):609–628, 1994.
- [13] S. Chen, P. M. Grant, S. McLaughlin, and B. Mulgrew. Complex-Valued Radial Basis Function Networks. In *Proc. Third IEE Int'l Conf. Artif. Neural Networks*, pages 148–152, May 1993.

- [14] J. Anderson, J. Platt, and D. Kirk. *An Analog VLSI Chip for Radial Basis Functions*, pages 765–772. Morgan Kaufmann, 1993.
- [15] M. A. Neifeld and D. Psaltis. Optical implementations of radial basis classifiers. *Appl. Opt.*, 32(08):1370–1379, 10 Mar 1993.
- [16] M. T. Musavi, W. Ahmed, K. H. Chan, K. B. Faris, and D. M. Hummels. On the Training of Radial Basis Function Classifiers. *Neural Networks*, 5:595–603, 1992.
- [17] J. S. Denker, W. R. Gardner, H. P. Graf, D. Henderson, R. E. Howard, W. Hubbard, L. D. Jackel, H. S. Baird, and I. Guyon. Neural Network Recognizer for Hand-written ZIP Code Digits. In D. S. Touretzky, editor, *Adv. in Neural Info. Proc. Systems*, volume 1, pages 323–331, 1989.
- [18] M. A. Neifeld, S. Rakshit, A. Yamamura, S. Kobayashi, and D. Psaltis. Optical disk implementation of radial basis classifiers. In *Proc. of SPIE*, volume 1347, pages 4–15, 1990.
- [19] D. A. Jared, K. M. Johnson, and G. Moddel. Joint transform correlator using an amorphous silicon ferroelectric liquid crystal spatial light modulator. *Opt. Commun.*, 76(2):97–102, 1990.
- [20] B. K. Taylor and D. P. Casasent. Error-source effects in a high-accuracy optical finite-element processor. *Appl. Opt.*, 25(6):966–975, 1986.
- [21] C. S. Sexton. Current Status of Hughes Liquid Crystal Light Valve Performance for Optical Data Processing. In *Proc. of SPIE*, volume 684, pages 96–100, 1986.
- [22] T. Masters. *Signal and Image Processing with Neural Networks*. Wiley, 1994.
- [23] T. O'Donnell, J. Simmers, and H. Southall. An Introduction to Neural Beamforming. In *IEEE Dual-Use Technologies and Applications Conference*, volume I, pages 483–492, May 1994.
- [24] J. Simmers, H. Southall, and T. O'Donnell. Advances in Neural Beamforming. In *Proc. of the 1993 Antenna Applications Symposium*, volume 1, pages 203–216, Univ. of Illinois, Sep 1993.
- [25] T. O'Donnell, J. Simmers, and D. Jacavanco. Neural Beamforming for Phased-Array Antennas. In *Proc. of the 1992 Antenna Applications Symposium*, volume 1, pages 106–115, University of Illinois, Sep 1992.
- [26] J. Simmers and T. O'Donnell. Adaptive RBF Neural Beamforming. In *IEEE Command, Control, Communications and Intelligence Technology Applications Conference*, pages 94–98, June 1992.

Rome Laboratory
Customer Satisfaction Survey

RL-TR-_____

Please complete this survey, and mail to RL/IMPS,
26 Electronic Pky, Griffiss AFB NY 13441-4514. Your assessment and
feedback regarding this technical report will allow Rome Laboratory
to have a vehicle to continuously improve our methods of research,
publication, and customer satisfaction. Your assistance is greatly
appreciated.

Thank You

Organization Name: _____ (Optional)

Organization POC: _____ (Optional)

Address: _____

1. On a scale of 1 to 5 how would you rate the technology
developed under this research?

5-Extremely Useful 1-Not Useful/Wasteful

Rating _____

Please use the space below to comment on your rating. Please
suggest improvements. Use the back of this sheet if necessary.

2. Do any specific areas of the report stand out as exceptional?

Yes _____ No _____

If yes, please identify the area(s), and comment on what
aspects make them "stand out."

3. Do any specific areas of the report stand out as inferior?

Yes No

If yes, please identify the area(s), and comment on what aspects make them "stand out."

4. Please utilize the space below to comment on any other aspects of the report. Comments on both technical content and reporting format are desired.

***MISSION
OF
ROME LABORATORY***

Mission. The mission of Rome Laboratory is to advance the science and technologies of command, control, communications and intelligence and to transition them into systems to meet customer needs. To achieve this, Rome Lab:

- a. Conducts vigorous research, development and test programs in all applicable technologies;
- b. Transitions technology to current and future systems to improve operational capability, readiness, and supportability;
- c. Provides a full range of technical support to Air Force Materiel Command product centers and other Air Force organizations;
- d. Promotes transfer of technology to the private sector;
- e. Maintains leading edge technological expertise in the areas of surveillance, communications, command and control, intelligence, reliability science, electro-magnetic technology, photonics, signal processing, and computational science.

The thrust areas of technical competence include: Surveillance, Communications, Command and Control, Intelligence, Signal Processing, Computer Science and Technology, Electromagnetic Technology, Photonics and Reliability Sciences.